Study of the $\Delta(1232)$ using single and double polarization asymmetries

A. Biselli,[1,*] G.S. Adams,[1] M.J. Amaryan,[36] E. Anciant,[24] M. Anghinolfi,[2] D.S. Armstrong,[7] B. Asavapibhop,[27] G. Asryan,[36] G. Audit,[24] T. Auger,[24] H. Avakian,[13] S. Barrow,[11] M. Battaglieri,[2] K. Beard,[16] M. Bektasoglu,[21] B.L. Berman,[12] W. Bertozzi,[19] N. Bianchi,[13] S. Boiarinov,[14] B.E. Bonner,[23] P. Bosted,[27] S. Bouchigny,[17] D. Branford,[9] W.J. Briscoe,[12] W.K. Brooks,[17] S. Bueltmann,[34] V.D. Burkert,[17] J.R. Calarco,[29] G.P. Capitani,[13] D.S. Carman,[22] B. Carnahan,[5] C. Cetina,[12] L. Ciciani,[21] R. Clark,[4] P.L. Cole,[33] A. Coleman,[7] J. Connelly,[12] D. Cords,[17] P. Corvisiero,[2] D. Crabb,[34] H. Crannell,[5] J. Cummings,[1] E. De Sanctis,[13] R. De Vita,[2] P.V. Degtyarenko,[17] R.A. Demirchyan,[36] H. Denizli,[30] L.C. Dennis,[11] A. Deppman,[13] K.V. Dharmawardane,[21] K.S. Dhuga,[12] C. Djalali,[32] G.E. Dodge,[21] J. Domingo,[17] D. Doughty,[6,17] P. Dragovitsch,[11] M. Dugger,[3] S. Dytman,[30] M. Eckhause,[7] Y.V. Efremenko,[14] H. Egiyan,[7] K.S. Egiyan,[36] L. Elouadrhiri,[6,17] A. Empl,[1] L. Farhi,[24] R. Fatemi,[34] R.J. Feuerbach,[4] J. Ficenec,[35] K. Fissum,[19] T.A. Forest,[21] A. Freyberger,[17] V. Frolov,[1] H. Funsten,[7] S.J. Gaff,[8] M. Gai,[26] G. Gavalian,[36] V.B. Gavrilov,[14] S. Gilad,[19] G.P. Gilfoyle,[31] K.L. Giovanetti,[16] P. Girard,[32] E. Golovatch,[28] K.A. Griffioen,[7] M. Guidal,[15] M. Guillo,[32] V. Gyurjyan,[17] D. Hancock,[7] J. Hardie,[6] D. Heddle,[6,17] P. Heimberg,[12] J. Heisenberg,[29] F.W. Hersman,[29] K. Hicks,[22] R.S. Hicks,[27] M. Holtrop,[29] J. Hu,[1] C.E. Hyde-Wright,[21] M.M. Ito,[17] D. Jenkins,[35] K. Joo,[34] J.H. Kelley,[8] M. Khandaker,[20,17] K.Y. Kim,[30] D.H. Kim,[18] K. Kim,[18] W. Kim,[18] A. Klein,[21] F.J. Klein,[17] M. Klusman,[1] M. Kossov,[14] L.H. Kramer,[10,17] Y. Kuang,[7] J. Kuhn,[1] S.E. Kuhn,[21] J.M. Laget,[24] D. Lawrence,[27] G.A. Leksin,[14] A. Longhi,[5] K. Loukachine,[35] M. Lucas,[32] R.W. Major,[31] J.J. Manak,[17] C. Marchand,[24] S.K. Matthews,[5] L.C. Maximon,[12] S. McAleer,[11] J.W.C. McNabb,[4] J. McCarthy,[34] B.A. Mecking,[17] M.D. Mestayer,[17] C.A. Meyer,[4] R. Minehart,[34] M. Mirazita,[13] R. Miskimen,[27] V. Mokeev,[28] V. Muccifora,[13] J. Mueller,[30] L.Y. Murphy,[12] G.S. Mutchler,[23] J. Napolitano,[1] S.O. Nelson,[8] G. Niculescu,[22] B. Niczyporuk,[17] R.A. Niyazov,[21] J.T. O'Brien,[5] G.V. O'Rielly,[12] M.S. Ohandjanyan,[36] A. Opper,[22] M. Ossipenko,[28] K. Park,[18] Y. Patois,[32] G.A. Peterson,[27] S. Philips,[12] N. Pivnyuk,[14] D. Pocanic,[34] O. Pogorelko,[14] E. Polli,[13] B.M. Preedom,[32] J.W. Price,[25] L.M. Qin,[21] B.A. Raue,[10,17] A.R. Reolon,[13] G. Riccardi,[11] G. Ricco,[2] M. Ripani,[2] B.G. Ritchie,[3] S. Rock,[27] F. Ronchetti,[13] P. Rossi,[13] D. Rowntree,[19] P.D. Rubin,[31] K. Sabourov,[8] C.W. Salgado,[20] M. Sanzone,[13] V. Sapunenko,[2] M. Sargsyan,[36] R.A. Schumacher,[4] V.S. Serov,[14] A. Shafi,[12] Y.G. Sharabian,[36] J. Shaw,[27] S.M. Shuvalov,[14] S. Simionatto,[12] A. Skabelin,[19] E.S. Smith,[17] L.C. Smith,[34] T. Smith,[29] D.I. Sober,[5] L. Sorrell,[27] M. Spraker,[8] S. Stepanyan,[36,21] P. Stoler,[1] I.I. Strakovsky,[12] M. Taiuti,[2] S. Taylor,[23] D. Tedeschi,[32] R. Thompson,[30] L. Todor,[4] T.Y. Tung,[7] M.F. Vineyard,[31] A. Vlassov,[14] K. Wang,[34] L.B. Weinstein,[21] A. Weisberg,[22] H. Weller,[8] R. Welsh,[7] D.P. Weygand,[17] S. Whisnant,[32] M. Witkowski,[1] E. Wolin,[17] L. Yanik,[12] A. Yegneswaran,[17] J. Yun,[21] B. Zhang,[19] J. Zhao,[19] and Z. Zhou[19]

(The CLAS Collaboration)

[1]*Rensselaer Polytechnic Institute, Department of Physics, Troy, NY 12181, USA*
[2]*Istituto Nazionale di Fisica Nucleare, Sezione di Genova e Dipartimento di Fisica dell'Universita, 16146 Genova, Italy*
[3]*Arizona State University, Department of Physics and Astronomy, Tempe, AZ 85287, USA*
[4]*Carnegie Mellon University, Department of Physics, Pittsburgh, PA 15213, USA*
[5]*Catholic University of America, Department of Physics, Washington D.C., 20064, USA*
[6]*Christopher Newport University, Newport News, VA 23606, USA*
[7]*College of William and Mary, Department of Physics, Williamsburg, VA 23187, USA*
[8]*Duke University, Physics Bldg. TUNL, Durham, NC27706, USA*
[9]*Department of Physics and Astronomy, Edinburgh University, Edinburgh EH9 3JZ, United Kingdom*
[10]*Florida International University, Miami, FL 33199, USA*
[11]*Florida State University, Department of Physics, Tallahassee, FL 32306, USA*
[12]*George Washington University, Department of Physics, Washington D. C., 20052 USA*
[13]*Istituto Nazionale di Fisica Nucleare, Laboratori Nazionali di Frascati, P.O. 13, 00044 Frascati, Italy*
[14]*Institute of Theoretical and Experimental Physics, 25 B. Cheremushkinskaya, Moscow, 117259, Russia*
[15]*Institut de Physique Nucleaire d'Orsay, IN2P3, BP 1, 91406 Orsay, France*
[16]*James Madison University, Department of Physics, Harrisonburg, VA 22807, USA*
[17]*Thomas Jefferson National Accelerator Facility, 12000 Jefferson Avenue, Newport News, VA 23606, USA*
[18]*Kyungpook National University, Department of Physics, Taegu 702-701, South Korea*
[19]*M.I.T.-Bates Linear Accelerator, Middleton, MA 01949, USA*
[20]*Norfolk State University, Norfolk VA 23504, USA*
[21]*Old Dominion University, Department of Physics, Norfolk VA 23529, USA*
[22]*Ohio University, Department of Physics, Athens, OH 45701, USA*
[23]*Rice University, Bonner Lab, Box 1892, Houston, TX 77251, USA*
[24]*CEA Saclay, DAPNIA-SPhN, F91191 Gif-sur-Yvette Cedex, France*
[25]*University of California at Los Angeles, Department of Physics and Astronomy, Los Angeles, CA 90095-1547, USA*

[26] University of Connecticut, Physics Department, Storrs, CT 06269, USA
[27] University of Massachusetts, Department of Physics, Amherst, MA 01003, USA
[28] University of Moscow, Moscow, 119899 Russia
[29] University of New Hampshire, Department of Physics, Durham, NH 03824, USA
[30] University of Pittsburgh, Department of Physics and Astronomy, Pittsburgh, PA 15260, USA
[31] University of Richmond, Department of Physics, Richmond, VA 23173, USA
[32] University of South Carolina, Department of Physics, Columbia, SC 29208, USA
[33] University of Texas at El Paso, Department of Physics, El Paso, Texas 79968, USA
[34] University of Virginia, Department of Physics, Charlottesville, VA 22903, USA
[35] Virginia Polytechnic and State University, Department of Physics, Blacksburg, VA 24061, USA
[36] Yerevan Physics Institute, 375036 Yerevan, Armenia

(Dated: February 5, 2003)

Measurement of the angular distributions of target and double spin asymmetries for the $\Delta^+(1232)$ in the exclusive channel $\vec{p}(\vec{e},e',p)\pi^0$ obtained at Jefferson Lab in the Q^2 range from 0.5 to 1.5 GeV$^2/c^2$ are presented. Results of the asymmetries are compared with the unitary isobar model MAID , the dynamical model by Sato and Lee and the effective Lagrangian theory by R. Davidson and N. Mukhopadhyay. Sensitivity to the different models was observed, particularly in relation to the description of background terms E_{0+}, S_{0+}, M_{1+} and S_{1-}, on which the target asymmetry depends significantly.

PACS numbers:

I. INTRODUCTION

The $\Delta(1232)$ resonance has been one of the most studied resonances in particle and nuclear physics. As the lowest energy nucleon excitation it dominates the low energy cross sections for pion- and electromagnetic-induced reactions, and is almost completely separated in excitation energy from the many broad higher mass resonances. There is an extensive theoretical literature attempting to characterize the electromagnetic excitation of the $\Delta(1232)$. For example, some approaches are: effective Lagrangian [1–6], dispersion relations [7], Quark model [8, 9],QCD sum-rule approach [10], or the generalized parton distribution (GPD) approach [11, 12], and perturbative QCD with QCD sum-rules [13]. In recent years considerable experimental activity was undertaken using polarized real photons at LEGS [14] and Mainz [15], unpolarized electrons at Bonn [16] and Jefferson Lab (JLab) [17] [18], and polarized electrons at Bates [19] and JLab [20], which have focused on constraining our understanding of the electromagnetic structure of the $\Delta(1232)$.

Experiments utilizing polarized beams and/or targets are of particular interest since they allow one to test and constrain effective field theories which can completely predict the electro-production cross section by fitting only unpolarized electro- and photo-production data. In the case of resonances the terms that arise in the cross-section when target or beam are polarized are especially interesting since they depend on the interference with the background and, for the $\Delta(1232)$, are not dominated by the $|M_{1+}|^2$ (see Appendix for notation) as in the case of the unpolarized cross-section.

The reaction studied in the present article is $\vec{e}+\vec{p}\to e'+p+\pi^0$, where the scattered electron and emitted proton were observed in coincidence, and the π^0 was identified by the missing mass technique. This is the first exclusive measurement with both target protons and incident electrons polarized. Target and double spin asymmetries were extracted and compared to the predictions of the unitary isobar model MAID [5], the dynamical model by Sato and Lee [2] and the effective Lagrangian theory by R. Davidson and N.Mukhopadhyay [6]. These three theories start with an effective Lagrangian but they differ significantly in the calculation of pion multiple scattering and in the implementation of the unitarization condition.

II. FORMALISM.

The five-fold differential cross section for single meson production schematically shown in Figure 1 can be written as

$$\frac{d\sigma}{d\epsilon_f d\Omega_e d\Omega^*} = \Gamma\frac{d\sigma}{d\Omega^*} \tag{1}$$

where

$$\Gamma = \frac{\alpha}{2\pi^2}\frac{\epsilon_f}{\epsilon_i}\frac{k_\gamma^{lab}}{Q^2}\frac{1}{1-\epsilon} \tag{2}$$

is the virtual photon flux,

$$\epsilon = (1+2\frac{|\vec{q}\,|^2}{Q^2}\tan^2\frac{\theta_e}{2})^{-1} \tag{3}$$

represents the degree of polarization of the virtual photon,

$$k_\gamma^{lab} = \frac{W^2-M^2}{2M} \tag{4}$$

*Contact Author `biselli@jlab.org`

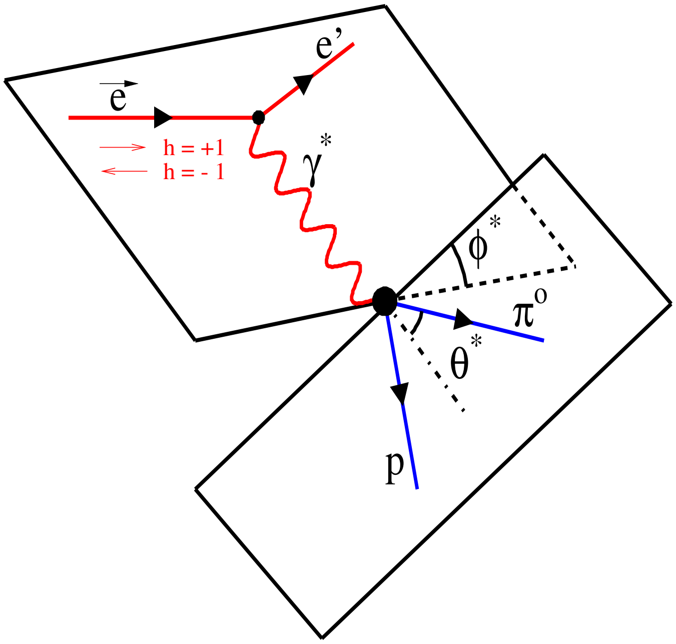

FIG. 1: Schematic diagram of π nucleon electro-production.

denotes the 'photon equivalent energy' necessary for a real photon to excite a hadronic system with c.m. energy W, and $Q^2 = -q^2 = -(\omega^2 - \vec{q}^2)$ is the momentum transfer. The differential cross section for pion production by a virtual photon $d\sigma/d\Omega^*$ can be written as a sum of four terms as follows:

$$\frac{d\sigma}{d\Omega^*} = \frac{|\vec{k}|}{k_\gamma^{cm}}\left\{\frac{d\sigma_0}{d\Omega^*} + h\frac{d\sigma_e}{d\Omega^*} + P\frac{d\sigma_t}{d\Omega^*} - hP\frac{d\sigma_{et}}{d\Omega^*}\right\} \quad (5)$$

where h and P are the target and beam polarization, respectively. The first term $d\sigma_0/d\Omega^*$ represents the unpolarized cross section, while the remaining terms $d\sigma_e/d\Omega^*$, $d\sigma_t/d\Omega^*$ and $d\sigma_{et}/d\Omega^*$ arise when beam, target or both beam and target are polarized, respectively. Here

$$k_\gamma^{cm} = \frac{M}{W}k_\gamma^{lab} \quad (6)$$

is the 'real photon equivalent energy' in the cm frame. These cross-sections can be written in terms of response functions R [21],

$$\begin{aligned}
\frac{d\sigma_0}{d\Omega^*} =& R_T^0 + \epsilon_L R_L^0 + \sqrt{2\epsilon_L(1+\epsilon)}R_{TL}^0\cos\phi^* + \epsilon R_{TT}^0\cos 2\phi^* \\
\frac{d\sigma_e}{d\Omega^*} =& \sqrt{2\epsilon_L(1-\epsilon)}R_{TL'}^0\sin\phi^* \\
\frac{d\sigma_t}{d\Omega^*} =& \sin\theta_\gamma\cos\phi^*[\sqrt{2\epsilon_L(1+\epsilon)}R_{TL}^x\sin\phi^* + \epsilon R_{TT}^x\sin 2\phi^*] + \sin\theta_\gamma\sin\phi^*[R_{TL}^y + \epsilon_L R_L^y + \\
&+ \sqrt{2\epsilon_L(1+\epsilon)}R_{TL}^y\cos\phi^* + \epsilon R_{TT}^y\cos 2\phi^*] + \cos\theta_\gamma[\sqrt{2\epsilon_L(1+\epsilon)}R_{TL}^z\sin\phi^* + \epsilon R_{TT}^z\sin 2\phi^*] \\
\frac{d\sigma_{et}}{d\Omega^*} =& -\sin\theta_\gamma[\sqrt{2\epsilon_L(1-\epsilon)}R_{TL'}^x\cos\phi^{*2} + \sqrt{1-\epsilon^2}R_{TT'}^x\cos\phi^*] + \sin\theta_\gamma\sqrt{2\epsilon_L(1-\epsilon)}R_{TL'}^y\sin\phi^{*2} \\
&-\cos\theta_\gamma[\sqrt{2\epsilon_L(1-\epsilon)}R_{TL'}^z\cos\phi^* + \sqrt{1-\epsilon^2}R_{TT'}^z]
\end{aligned} \quad (7)$$

where

$$\epsilon_L = \frac{Q^2}{\omega^2}\epsilon \quad (8)$$

is the frame dependent longitudinal polarization. The terms $\sin\theta_\gamma$ and $\cos\theta_\gamma$ represent projections of the target polarization with respect to the virtual photon momentum vector.

The asymmetries are then defined as follows:

$$\begin{aligned}
A_e =& \frac{\sigma_e}{\sigma_0} \\
A_t =& \frac{\sigma_t}{\sigma_0} \\
A_{et} =& \frac{\sigma_{et}}{\sigma_0}
\end{aligned} \quad (9)$$

where $\sigma_0 \equiv d\sigma_0/d\Omega^*$, $\sigma_e \equiv d\sigma_e/d\Omega^*$, $\sigma_t \equiv d\sigma_t/d\Omega^*$ and $\sigma_{et} \equiv d\sigma_{et}/d\Omega^*$.

III. EXPERIMENTAL SETUP.

The experiment was carried out from September to December 1998 using the CEBAF Large Acceptance Spectrometer (CLAS) at the Thomas Jefferson National Accelerator Facility, using a polarized electron beam of energy $E = 2.565$ GeV at an average beam current of about 2 nA. A pair of complementary helicity states were created pseudo-randomly by a rotatable pockel cell placed in front of the the circularly polarized laser light used to produce polarized electrons from a strained GaAs crystal [22]. Each pair of complementary helicity states has a duration of 2 sec. Helicity correlated systematic errors are reduced by selecting the helicity pair pseudo-randomly. The polarization of the beam, measured with a Møller polarimeter, was $h = 0.71 \pm 0.01$. The beam was rastered in a spiral pattern of 1-1.2 cm over the surface of the target to avoid destroying the target polarization.

The electrons impinged on a solid ammonia (NH_3) target of thickness 530 mg/cm^2, in which the three protons were longitudinally polarized. The polarization was changed every 2-3 weeks. *Dynamic nuclear polarization* (DNP)[23, 24] was used to polarize this target using a 5 T uniform holding field generated by a super-conducting Helmholtz-like coil placed axially around the target. This coil limited the available scattering angles to less than 45° and between 70° and 110°. A more complete description of the target and polarization technique may be found in [25, 26]. Typically, the achieved polarizations for positive and negative polarizations was about 39% and 55%, respectively. The effective instantaneous luminosity for the polarized Hydrogen was about $6.6 \times 10^{32}\ cm^{-2}s^{-1}$.

Scattered electrons and recoiled protons were detected in the CLAS, which is described in detail in ref. [27, 28]. An event was triggered when a coincidence between the threshold Cherenkov counter (CC) [29] and the electromagnetic calorimeter (EC) [30] signals was detected. A typical Cherenkov signal consisted of 6 to 12 photoelectrons (PE), with an average of about 10. The trigger threshold was set at 0.5 PE. Electron candidates were identified by a combination of time of flight (TOF) scintillators, CC, and EC. The TOF scintillators completely surround the drift chambers whereas the EC and the CC subtend angles less than 45° with respect to the beam line. The momenta of the detected particles were determined by fitting their measured trajectories in a toroidal field, which curves the tracks in the θ direction but leaves them nearly unaffected in the ϕ direction. The trajectories are determined by 3 sets of drift chambers (DC), the inner most having 10 layers and each outer one having 12 layers of drift cells.

IV. DATA REDUCTION AND ANALYSIS

Electron identification. Electron identification was improved offline in order to remove pions and other sources of contamination. The EC signal was used to remove events in which tracks triggered the CC but did not shower in the EC, such as energetic pions. The energy released by electrons traversing the EC is proportional to the momentum p as shown in Figure 2(a). The band is due to EC resolution and the lines indicate the cut applied to remove background. The EC signal is also measured separately for the inner part (15 layers of scintillators) and outer part (24 layers). This allows one to distinguish between an electron, which showers mostly in the inner part, and minimum ionizing particles, such as π's, which lose most of their energy in the outer part or pass through without interacting. This behavior is evident in Figure 2(b) where the high intensity region with $E_{in} \sim E_{tot}$ are electrons, while the small peak at low E_{in} corresponds to misidentified pions. The line indicates the cut applied to remove misidentified pions.

The reconstructed vertex position was used to remove events originating from the temperature shields and the beam line exit window. Figure 3 shows the cut applied to selected events from inside the target.

Proton identification. Protons were identified by determining their momentum and path length using the DC, and their $\beta = v/c$ using the TOF. Figure 4 shows the cut applied to select protons, which appear well separated from the pions for momenta less than 2 GeV/c.

Channel identification. In order to select the $\Delta(1232)$ resonance in the decay channel $\Delta^+ \rightarrow \pi^0 p$, cuts on the invariant mass $W = |e + P - e'|$ and the square of the missing mass $M_X^2 = |e+P-e'-P'|^2$ were performed. The target used, $^{15}NH_3$, intrinsically has a large background due to scattering from bound nucleons in ^{15}N . Many of these events were removed through kinematic cuts. An initial 2-dimensional cut was applied to select the $\Delta(1232)$ region and to remove the elastic and quasi-elastic events as shown in Figure 5(a). The underlying quasi-Δ events from ^{15}N , not kinematically separable, were removed by a subtraction process by comparing to data taken with a ^{12}C target. Figure 5(b) shows the missing mass spectrum obtained with $^{15}NH_3$ and ^{12}C targets after the 2-dimensional cut and the resulting subtraction. The remaining pion peak due to the H is narrower than the $^{15}NH_3$ peak. A second and much tighter cut on M_X^2 alone was therefore performed to optimize the selection of pions from reactions on free hydrogen in $^{15}NH_3$. The two vertical lines in Figure 5(b) show the applied cut.

Elastic radiative tail. The elastic radiative tail was suppressed by the presence of the target magnetic coils which block polar angles between 45° and 70°. The remaining elastic radiative events were removed by means of a cut on the reconstructed electron scattered angle (θ) [31]. This cut removed 15% of the original data set.

Fiducial cuts and acceptance corrections. The efficiency can vary by more than an order of magnitude near the boundaries of the six azimuthal sectors of CLAS, therefore only events in the region where the acceptance is uniform were included. Limiting electrons to this *fiducial* region, gives an elastic scattering cross section that is consistent with the World's data to within a few percent (see ref [29]). Although the objective of the present analysis is to extract asymmetries, a good understanding of the acceptance is necessary. The asymmetries defined in equation 11 are integrated over ranges in Q^2, ϕ^*, θ^* and W and since the acceptance is a function of these variables, it does not cancel out when the ratio of the two integrals is taken. Fiducial cuts define a region in θ and ϕ depending on the momentum for both the electron and proton. The data inside the line in Figure 6(a) is an example of the region selected by the fiducial cuts for electrons detected in the first sector and with momenta between 1.9 GeV/c and 2.1 GeV/c. The cuts not only remove data close to the sector boundaries but further remove events from regions where scintillators are inefficient or have other tracking inefficiencies. Figure 6(b) displays the effect of a cut to remove an inefficient scintillator in the third sector. The total amount of data

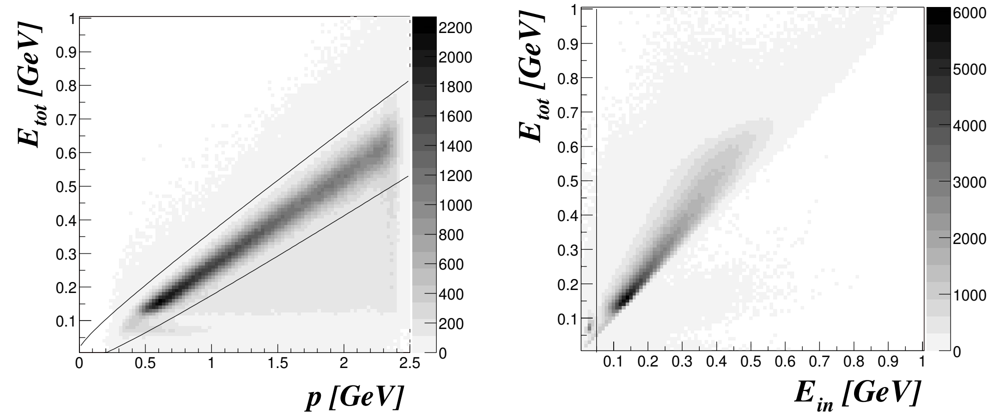

(a) $E_{tot}\ vs\ p$

(b) $E_{tot}\ vs\ E_{in}$

FIG. 2: Electron identification a)The two lines indicate the cut applied to remove events which deviate by more than three sigma from the expected behavior. b)The line indicates the cut applied to remove events that have E_{in} much smaller than E_{tot} which correspond to misidentified pions.

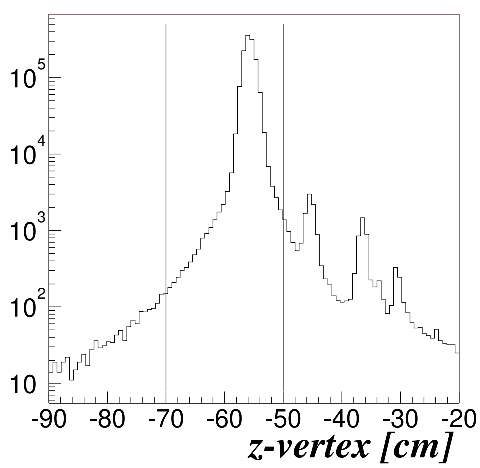

FIG. 3: Vertex z-position of the electron where z is along the beamline. The lines, which indicate the applied cut, show that the peaks coming from the scattering off temperature shields and the beam line exit window are completely removed. (Note log. vertical scale). The cut does not remove the exit and entrance windows from the target cell.

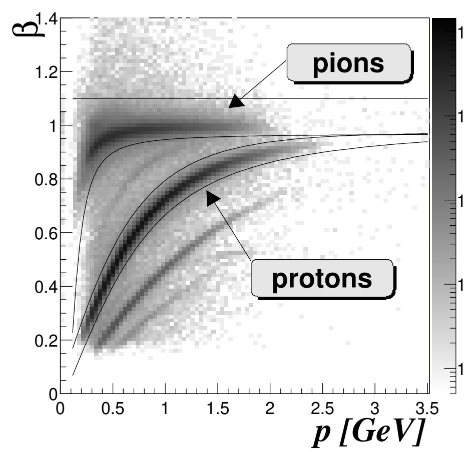

FIG. 4: $\beta\ vs\ p$ for all positive charge particles. The lines show how pions and protons are easily distinguishable.

removed by the fiducial cuts for events with one electron and one proton and $W < 1.4$ GeV/c^2 is on the order of 60%. Data were acceptance corrected event by event using an analytical calculation which was based on the assumption that acceptance within the fiducial region is 100%. Figure 7 shows the acceptance as a function of ϕ^* and θ^* calculated for two intervals in Q^2 within a W range from 1.1 GeV/c^2 to 1.3 GeV/c^2.

Experimental definition of the asymmetries. The quantities experimentally measured, N_{ij}, are grouped according to different combinations of beam (i) and target (j) polarizations. Under the assumption of constant efficiency, these may be written in terms of the cross sections in equations 7 as:

$$\begin{aligned}
N_{\uparrow\uparrow} &\propto (\sigma_0 + \sigma_0^N + h\sigma_e + h\sigma_e^N + P^a\sigma_t - hP^a\sigma_{et}) \\
N_{\downarrow\uparrow} &\propto (\sigma_0 + \sigma_0^N - h\sigma_e - h\sigma_e^N + P^a\sigma_t + hP^a\sigma_{et}) \\
N_{\uparrow\downarrow} &\propto (\sigma_0 + \sigma_0^N + h\sigma_e + h\sigma_e^N - P^b\sigma_t + hP^b\sigma_{et}) \\
N_{\downarrow\downarrow} &\propto (\sigma_0 + \sigma_0^N - h\sigma_e - h\sigma_e^N - P^b\sigma_t - hP^b\sigma_{et})
\end{aligned} \tag{10}$$

where σ_0^N and σ_e^N are the contributions from the scattering from ^{15}N and the liquid helium coolant, and P^a and P^b are the positive and negative target polarizations, respectively. The left side of these equations (N_{ij}) has been normalized to the same total charge. The asymmetries

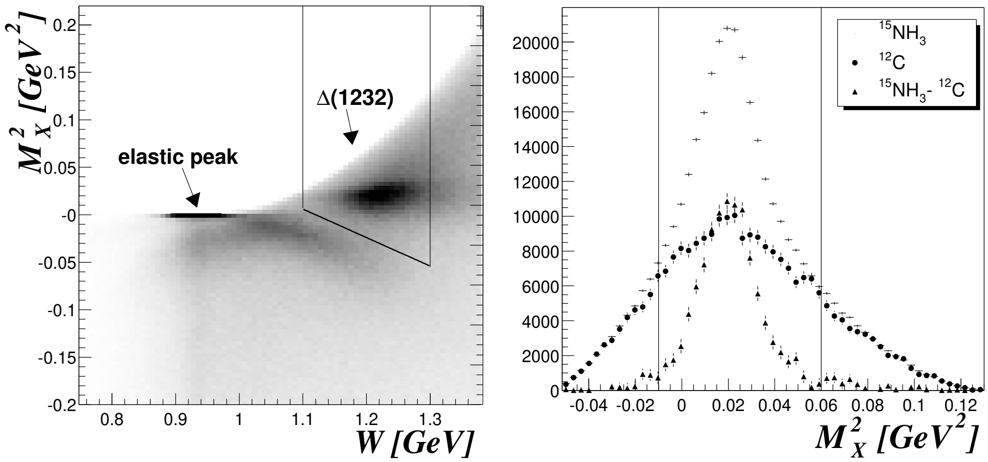

(a) M_X^2 vs W (b) M_X^2

FIG. 5: Identification of $p\pi^0$ events. The left plot shows the two-dimensional cut applied in order to remove the elastic events and quasi elastic shoulder. The right plot shows the resulting M_X^2 spectrum after the two-dimensional cut (dots), the ^{12}C data normalized to the $^{15}NH_3$ target data (full circles) and the subtraction of the two (triangles). The two lines show the final cut in M_X^2 to select pions coming from scattering off hydrogen.

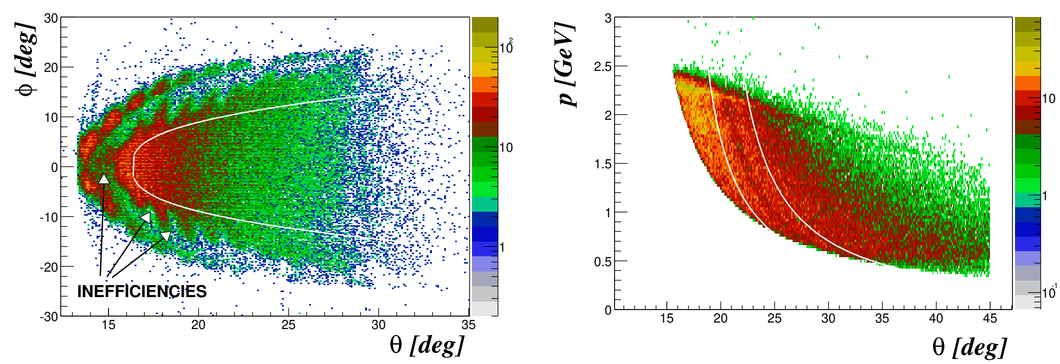

(a) (b)

FIG. 6: a)ϕ vs θ for electron in the first sector for a momentum bin 1.9 GeV/c $< p <$ 2.1 GeV/c. The line indicates the cut applied to remove the external fringes and the depletion due to CC inefficiencies. b)p vs θ for electron in the third sector after applying the cut shown in a). The region inside the two lines corresponds to a inefficient scintillator.

may be written in terms of these quantities as

$$A_t = \frac{\sigma_t}{\sigma_0} = \frac{1}{P^b}\frac{(N_{\uparrow\uparrow}+N_{\downarrow\uparrow})+(N_{\uparrow\downarrow}+N_{\downarrow\downarrow})}{(N_{\uparrow\uparrow}+N_{\downarrow\uparrow})+\alpha(N_{\uparrow\downarrow}+N_{\downarrow\downarrow})-\sigma_0^N}$$
$$A_{et} = \frac{\sigma_{et}}{\sigma_0} = \frac{1}{hP^b}\frac{-(N_{\uparrow\uparrow}-N_{\downarrow\uparrow})+(N_{\uparrow\downarrow}-N_{\downarrow\downarrow})}{(N_{\uparrow\uparrow}+N_{\downarrow\uparrow})+\alpha(N_{\uparrow\downarrow}+N_{\downarrow\downarrow})-\sigma_0^N} \tag{11}$$

where

$$\alpha = \frac{P^a}{P^b} \tag{12}$$

The extraction of the nuclear background cross section σ_0^N and the constant α are discussed in the next two sections.

Background subtraction. The data have a large background σ_0^N due to scattering from ^{15}N and the helium cooling bath. Data taken with ^{12}C and ^4He targets were used to remove this contribution. While ^{12}C and ^{15}N have a similar radiation length, they displace different amounts of helium. A two step procedure to handle this problem was employed. The first step was to determine how to add ^{12}C and empty target data properly in order to have the same ratio of ^{15}N and helium in the $^{15}NH_3$ data. Using a calculation based on the target thicknesses, densities and windows con-

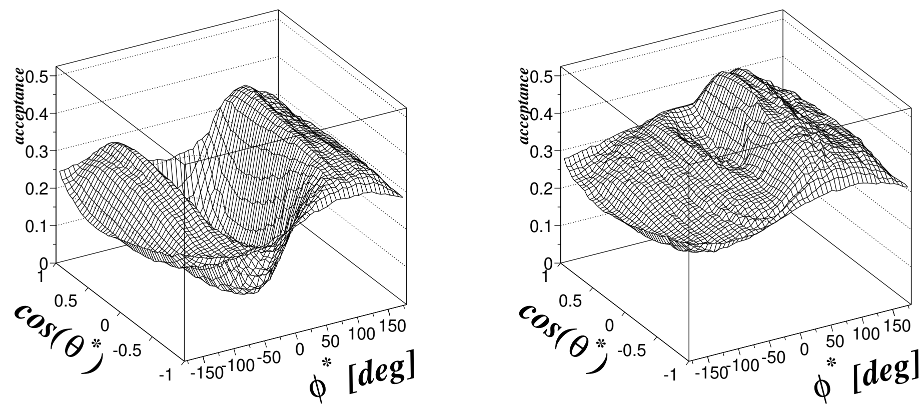

(a) $0.5\ \mathrm{GeV}^2/c^2 < Q^2 < 0.9\ \mathrm{GeV}^2/c^2$

(b) $0.9\ \mathrm{GeV}^2/c^2 < Q^2 < 1.5\ \mathrm{GeV}^2/c^2$

FIG. 7: Acceptance calculation for two intervals in Q^2 for $1.1\ \mathrm{GeV}/c^2 < W < 1.3\ \mathrm{GeV}/c^2$. The lower interval has a region around $\phi^* = 0°$ where the acceptance is zero.

tributions, the background spectrum was calculated as $N^{BG} = N^C - (0.331 \pm 0.008)N^E$, were N^C and N^E are the total number of ^{12}C and empty target data, normalized to the same charge.

The second step in the background subtraction was to determine a cross-normalization constant C_Δ, which allows N^{BG} to be equivalent to the rates from ^{15}N , accounting for the different ratio of protons to neutrons between the two backgrounds. A constant for the elastic region C_{el} was found as a ratio of the integrals of the W tails of the $^{15}NH_3$ and background data from $W = 0.6$ to $0.85\ \mathrm{GeV}/c^2$ where only events scattering by bound nucleons are present. Figure 8(a) shows the overlay of the W spectra of $^{15}NH_3$ and ^{12}C after normalization by C_{el}. A correction for higher W was then applied to C_{el} to account for rates from scattering off neutrons. $C_\Delta = \frac{6}{7}\frac{22}{18}C_{el}$ was obtained for the $\Delta(1232)$ region, where $\frac{6}{7}$ is the ratio of protons in ^{12}C and ^{15}N and $\frac{22}{18}$ is based on a Clebsch-Gordan coefficient analysis. Figure 8(b) shows the overlay of M_x^2 for $^{15}NH_3$ and background data after normalization using C_Δ. The tails where $M_x^2 < 0$ match as expected since they come only from quasi-elastic scattering off the bound nucleons. The technique was later verified using a ^{15}N target.

Target polarization measurement. The target polarization was extracted by comparing the well known elastic scattering asymmetry [32]

$$A_{theo} = -\frac{\cos\theta_\gamma\sqrt{1-\epsilon^2} + (\frac{Q^2}{4M^2})^{-\frac{1}{2}}\sqrt{2\epsilon(1-\epsilon)}\sin\theta_\gamma\cos\phi_\gamma\frac{G_E}{G_M}}{\epsilon(\frac{Q^2}{4M^2})^{-1}(\frac{G_E}{G_M})^2 + 1} \tag{13}$$

with the measured asymmetry

$$A_{meas} = \frac{N_{\uparrow\uparrow} - N_{\downarrow\uparrow}}{N_{\uparrow\uparrow} + N_{\downarrow\uparrow}} = \frac{hP\sigma_{et}}{\sigma_0} \equiv hPA_{theo} \tag{14}$$

The ratio $\frac{G_E}{G_M}$ has been measured in many experiments and it is known within a 3% accuracy in the Q^2 region of interest [33] The product of beam and target polarization (hP) was extracted in six Q^2 bins and then the average value was calculated. Figure 9 shows the results for the positive (hP^a) and negative target polarization data (hP^b). These measurements allow one to extract target polarizations P^a, P^b by simply taking the ratio of these products and the measured beam polarization h (see section III).

Systematic errors. Several sources of possible systematic effects were identified in the analysis procedure. To estimate the size of these errors, asymmetries were recalculated changing individual parameters in the analysis and comparing with the original result. Table I summarizes the systematic errors for A_{et} in the bin $0.9\ \mathrm{GeV}^2/c^2 < Q^2 < 1.5\ \mathrm{GeV}^2/c^2$. Similar values were found for the other asymmetries and Q^2 bins. The over-

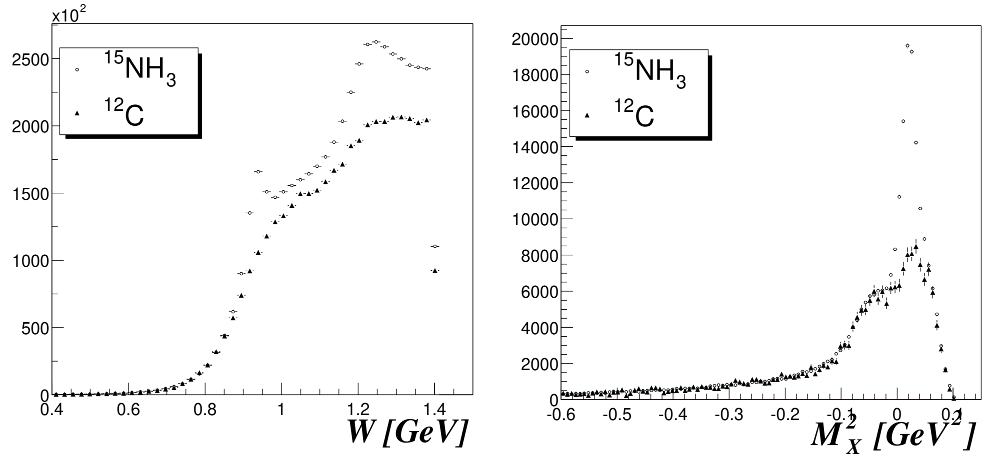

(a) (b)

FIG. 8: a)Exclusive W spectra for $^{15}NH_3$ (circles) and ^{12}C (triangles). The spectra are normalized to each other using the integrals of the W tails in the range 0.6 GeV$/c^2$ to 0.85 GeV$/c^2$.b)Overlay of M_X^2 spectra for $^{15}NH_3$ (circles) and ^{12}C (triangles). The ^{12}C was normalized using the constant found from the W tail integrals.

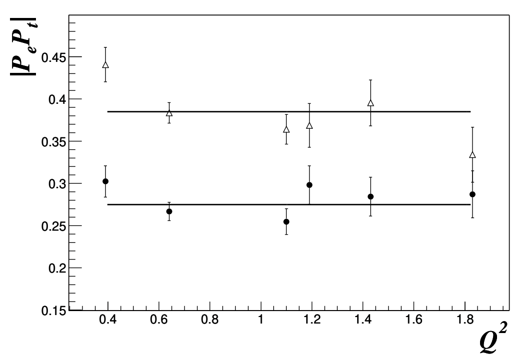

FIG. 9: The product $|P_eP_t|$ as a function of Q^2 for positive and negative target polarization runs. The six values for each polarization were fitted with a constant in order to obtain the average values $P_eP_t = 0.275 \pm 0.007$ and $P_eP_t = -0.385 \pm 0.008$. The χ^2/ndf values of the fits were 5.884/5 and 11.87/5 respectively.

all systematic error is on the order of 5% which is much smaller than the statistical error for the measured asymmetries.

Radiative corrections. Radiative corrections were estimated using a generalization of the Mo-Tsai formulation [34]. In particular the corrections were obtained by comparing Monte Carlo generated radiative and non-radiative events. The acceptance holes existing in the data were incorporated in the Monte Carlo in order to improve the model representation of the data. The difference between asymmetries calculated with radiative and non-radiative events revealed that radiative corrections influence the data by at most a few percent.

TABLE I: Summary of the systematic errors for the asymmetry A_{et} as a function of ϕ^* for 0.9 GeV$^2/c^2 < Q^2 <$ 1.5 GeV$^2/c^2$

Systematic error source	Systematic error (%)
Carbon normalization	4.2
P_eP_t	2.3
P_e	1.3
^4He background contribution	3.3
Norm const d	<-0.1

V. RESULTS.

Data for a beam energy of 2.565 GeV, within the $\Delta(1232)$ region (1.1 GeV$/c^2 < W <$ 1.3 GeV$/c^2$), span a range in momentum transfer from 0.4 GeV$^2/c^2$ to 1.5 GeV$^2/c^2$, as can be seen in Figure 10. The data were divided in two Q^2 bins, 0.5 GeV$^2/c^2 < Q^2 <$ 0.9 GeV$^2/c^2$ and 0.9 GeV$^2/c^2 < Q^2 <$ 1.5 GeV$^2/c^2$, and the asymmetries A_t and A_{et} were extracted according to the definitions in equations 11 as a function of the angles of the pion in the center of mass frame, ϕ^* and $\cos\theta^*$. The Q^2 dependences integrated over ϕ^* and $\cos\theta^*$ were extracted as well. The results are shown in Figures 11, 12 and 13 and listed in Table II, III, IV, V and VI. The beam asymmetry was not extracted because it could not be separated from the background stemming from $\Delta(1232)$ $\rightarrow \pi^- p$ which is produced by the scattering off neutrons in the ^{15}N .

According to Eq 7 the asymmetries depend on $\sin\phi$, $\cos\phi$, $\sin 2\phi$ and $\cos 2\phi$ giving a well defined functional dependence in ϕ which is model independent, and the data were found self-consistent in this respect. The target asymmetry was found to be an odd function and a fit to the function $\frac{A\cos\phi\sin\phi+B\sin\phi+C\sin^3\phi}{D+E\cos\phi+F\cos 2\phi}$ gave χ^2 per degree of freedom (ndf) values of 7.9/9 and 15.4/9 for the low and high Q^2 bin respectively. The double spin asymmetry was fitted with the even function $\frac{A+B\cos\phi+C\cos^2\phi}{D+E\cos\phi+F\cos 2\phi}$ and the values $\chi^2/ndf = 4.4/9$ for 0.5 GeV$^2/c^2 < Q^2 <$ 0.9 GeV$^2/c^2$ and 4.8/7 for 0.9 GeV$^2/c^2 < Q^2 <$ 1.5 GeV$^2/c^2$ were found.

Theoretical models. Four theoretical models were considered for this work: MAID2000, MAID98 [5] (MAID), an effective Lagrangian model developed by R. Davidson and N. Mukhopadhyay [6] (DM) and the dynamical model by Sato and Lee [1, 2] (SL). While these models all start with effective Lagrangians, differences arise in the calculations of pion multiple scattering and implementation of the the unitarity condition.

The MAID and DM models include pion scattering effects by using the K-matrix method to unitarize the amplitude. The differences between MAID and DM arise mainly from some rather significant differences in their starting effective Lagrangians. In particular, MAID uses a mixture of pseudo-scalar and pseudo-vector for the πNN coupling, while DM uses the standard pseudo-vector coupling. MAID includes some higher resonances and hence has more freedom in fitting the data.

The SL model obtains the unitary amplitudes by solving dynamical πN scattering equations. Thus the pion cloud effects on the extracted 'dressed' $N-\Delta$ can be identified and an interpretation of the resulting 'bare' parameters in terms of constituent quark model calculations has been established.

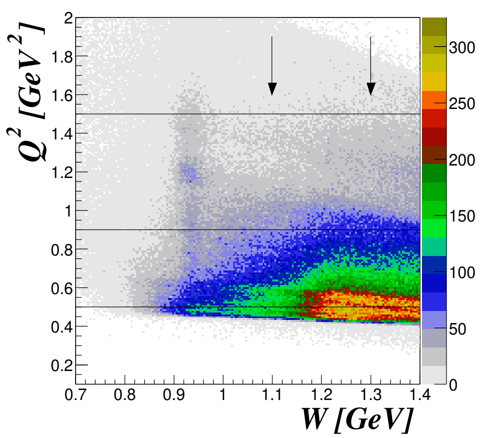

FIG. 10: Q^2 vs W. In the $\Delta(1232)$ region the accessible range in Q^2 is from 0.4 GeV$^2/c^2$ to 1.5 GeV$^2/c^2$. The horizontal lines delineate the two intervals of Q^2 in which the data were divided.

χ^2 comparison. The results were compared with these four models and satisfactory fits to the data were found in many cases. All the models predict the correct sign and the correct order of magnitude. A simultaneous χ^2 comparison of all angular, as well as the Q^2 distri-

TABLE II: Asymmetries A_t and A_{et} as a function of the center of mass angle of the pion ϕ^*.

$0.5 < Q^2 < 0.9$		
ϕ^*	A_t	A_{et}
-167.	$-0.108 \pm 0.063 \pm 0.008$	$-0.083 \pm 0.088 \pm 0.006$
-141.	$-0.271 \pm 0.058 \pm 0.018$	$-0.192 \pm 0.076 \pm 0.014$
-115.	$-0.266 \pm 0.044 \pm 0.016$	$-0.189 \pm 0.058 \pm 0.012$
-89.	$-0.071 \pm 0.036 \pm 0.006$	$-0.052 \pm 0.050 \pm 0.003$
-63.	$-0.191 \pm 0.083 \pm 0.012$	$-0.209 \pm 0.115 \pm 0.017$
0.	$-0.171 \pm 0.087 \pm 0.028$	$-0.433 \pm 0.136 \pm 0.026$
63.	$0.013 \pm 0.051 \pm 0.004$	$-0.211 \pm 0.074 \pm 0.016$
89.	$0.152 \pm 0.034 \pm 0.011$	$-0.079 \pm 0.047 \pm 0.004$
115.	$0.259 \pm 0.042 \pm 0.017$	$-0.172 \pm 0.055 \pm 0.012$
141.	$0.258 \pm 0.056 \pm 0.021$	$-0.232 \pm 0.075 \pm 0.020$
167.	$0.067 \pm 0.056 \pm 0.006$	$-0.172 \pm 0.080 \pm 0.014$

TABLE III: Asymmetries A_t and A_{et} as a function of the center of mass angle of the pion $\cos(\theta^*)$.

$0.5 < Q^2 < 0.9$		
$\cos(\theta^*)$	A_t	A_{et}
-0.938	$-0.061 \pm 0.096 \pm 0.038$	$-0.045 \pm 0.135 \pm 0.008$
-0.812	$0.113 \pm 0.078 \pm 0.0084$	$-0.336 \pm 0.119 \pm 0.044$
-0.688	$0.086 \pm 0.065 \pm 0.0032$	$-0.170 \pm 0.093 \pm 0.015$
-0.562	$0.087 \pm 0.068 \pm 0.0022$	$-0.165 \pm 0.097 \pm 0.014$
-0.438	$0.258 \pm 0.063 \pm 0.0182$	$-0.244 \pm 0.084 \pm 0.021$
-0.312	$0.243 \pm 0.068 \pm 0.0317$	$-0.139 \pm 0.089 \pm 0.012$
-0.188	$0.289 \pm 0.068 \pm 0.0171$	$-0.145 \pm 0.088 \pm 0.011$
-0.062	$0.155 \pm 0.055 \pm 0.0150$	$-0.298 \pm 0.080 \pm 0.017$
0.062	$0.262 \pm 0.051 \pm 0.0135$	$-0.181 \pm 0.068 \pm 0.010$
0.188	$0.210 \pm 0.057 \pm 0.0295$	$-0.114 \pm 0.077 \pm 0.006$
0.312	$0.200 \pm 0.047 \pm 0.0108$	$-0.174 \pm 0.064 \pm 0.010$
0.438	$0.239 \pm 0.058 \pm 0.0078$	$-0.172 \pm 0.077 \pm 0.010$
0.562	$0.146 \pm 0.058 \pm 0.0141$	$-0.280 \pm 0.084 \pm 0.018$
0.688	$0.174 \pm 0.052 \pm 0.0209$	$-0.178 \pm 0.072 \pm 0.012$
0.812	$0.110 \pm 0.058 \pm 0.0044$	$-0.005 \pm 0.080 \pm 0.002$
0.938	$0.006 \pm 0.063 \pm 0.0049$	$0.106 \pm 0.091 \pm 0.010$

TABLE IV: Asymmetries A_t and A_{et} as a function of the center of mass angle of the pion ϕ^*.

$0.9 < Q^2 < 1.5$		
ϕ^*	A_t	A_{et}
-167.143	$-0.056 \pm 0.129 \pm 0.004$	$-0.299 \pm 0.194 \pm 0.020$
-141.429	$-0.247 \pm 0.119 \pm 0.015$	$-0.178 \pm 0.160 \pm 0.012$
-115.714	$-0.250 \pm 0.096 \pm 0.015$	$-0.212 \pm 0.130 \pm 0.013$
-90.000	$-0.411 \pm 0.116 \pm 0.026$	$-0.146 \pm 0.136 \pm 0.011$
-64.286	$-0.504 \pm 0.162 \pm 0.053$	$-0.287 \pm 0.178 \pm 0.031$
-38.571	$-0.071 \pm 0.115 \pm 0.005$	$-0.070 \pm 0.162 \pm 0.006$
-12.857	$0.076 \pm 0.176 \pm 0.011$	$0.129 \pm 0.249 \pm 0.021$
12.857	$0.096 \pm 0.133 \pm 0.009$	$-0.325 \pm 0.202 \pm 0.033$
38.571	$-0.115 \pm 0.074 \pm 0.009$	$-0.271 \pm 0.107 \pm 0.020$
64.286	$0.095 \pm 0.067 \pm 0.006$	$-0.142 \pm 0.095 \pm 0.009$
90.000	$0.220 \pm 0.067 \pm 0.012$	$-0.156 \pm 0.090 \pm 0.009$
115.714	$0.189 \pm 0.067 \pm 0.011$	$-0.089 \pm 0.091 \pm 0.005$
141.429	$0.247 \pm 0.076 \pm 0.020$	$-0.179 \pm 0.101 \pm 0.014$
167.143	$0.295 \pm 0.089 \pm 0.015$	$-0.265 \pm 0.119 \pm 0.014$

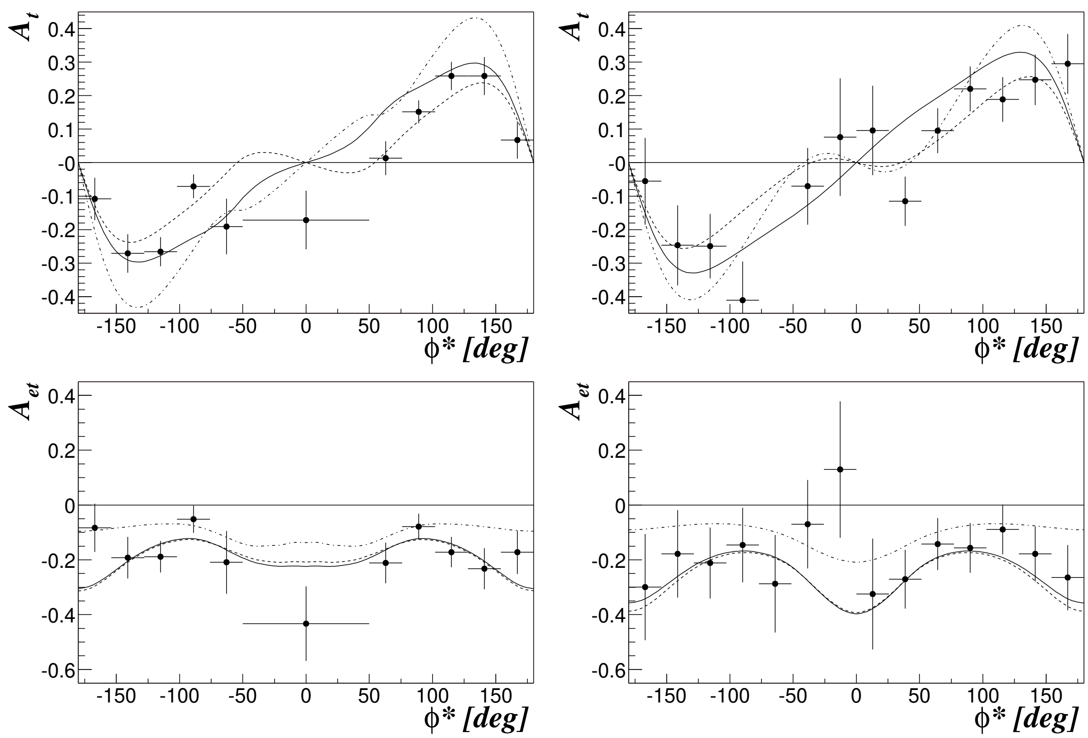

FIG. 11: Asymmetries A_t and A_{et} as a function of the center of mass angle of the pion ϕ^* for 0.5 GeV$^2/c^2 < Q^2 < 0.9$ GeV$^2/c^2$ (left) and 0.9 GeV$^2/c^2 < Q^2 < 1.5$ GeV$^2/c^2$ (right). The curves represent the predictions from the MAID2000 model (solid), Davidson-Mukhopadhyay model (dash-dotted) and Sato-Lee model (dashed). MAID98 was found to be very similar to MAID2000 and therefore it is not included in the graphs for the purpose of clarity.

TABLE V: Asymmetries A_t and A_{et} as a function of the center of mass angle of the pion $\cos(\theta^*)$.

$0.9 < Q^2 < 1.5$		
$\cos(\theta^*)$	A_t	A_{et}
-0.929	$0.281 \pm 0.271 \pm 0.002$	$0.322 \pm 0.366 \pm 0.096$
-0.786	$-0.100 \pm 0.120 \pm 0.008$	$-0.306 \pm 0.180 \pm 0.031$
-0.643	$-0.003 \pm 0.115 \pm 0.002$	$-0.512 \pm 0.196 \pm 0.049$
-0.500	$0.032 \pm 0.071 \pm 0.008$	$-0.203 \pm 0.103 \pm 0.016$
-0.357	$0.283 \pm 0.099 \pm 0.012$	$-0.420 \pm 0.141 \pm 0.029$
-0.214	$0.199 \pm 0.078 \pm 0.009$	$-0.212 \pm 0.107 \pm 0.011$
-0.071	$0.314 \pm 0.087 \pm 0.015$	$-0.154 \pm 0.112 \pm 0.007$
0.071	$0.279 \pm 0.081 \pm 0.009$	$-0.228 \pm 0.108 \pm 0.014$
0.214	$0.220 \pm 0.080 \pm 0.014$	$-0.171 \pm 0.109 \pm 0.008$
0.357	$0.228 \pm 0.094 \pm 0.019$	$-0.286 \pm 0.132 \pm 0.016$
0.500	$0.354 \pm 0.147 \pm 0.014$	$-0.135 \pm 0.176 \pm 0.011$
0.643	$0.158 \pm 0.075 \pm 0.008$	$-0.007 \pm 0.103 \pm 0.002$
0.786	$0.190 \pm 0.077 \pm 0.008$	$-0.113 \pm 0.105 \pm 0.007$
0.929	$0.390 \pm 0.169 \pm 0.008$	$0.239 \pm 0.203 \pm 0.025$

TABLE VI: Asymmetries A_t and A_{et} as a function of the momentum transfer Q^2.

$-1 < \cos\theta^* < 1$ $-180 < \phi^* < 180$		
Q^2	A_t	A_{et}
0.600	$0.171 \pm 0.019 \pm 0.014$	$-0.169 \pm 0.027 \pm 0.012$
0.800	$0.154 \pm 0.024 \pm 0.007$	$-0.146 \pm 0.033 \pm 0.010$
1.000	$0.205 \pm 0.036 \pm 0.008$	$-0.165 \pm 0.049 \pm 0.011$
1.200	$0.164 \pm 0.047 \pm 0.011$	$-0.207 \pm 0.066 \pm 0.012$
1.400	$0.223 \pm 0.059 \pm 0.017$	$-0.192 \pm 0.079 \pm 0.013$

butions was performed to establish quantitatively which model is the best description of the data. A χ^2 comparison for subsets of the experimental distributions was performed as well to understand the model sensitivity to the different asymmetries. In order for a χ^2 comparison to be made, the model prediction was disregarded where the acceptance was zero.

The χ^2 was defined as

$$\chi^2 = \sum_i \frac{(x_i^{\mathrm{data}} - x_i^{\mathrm{model}})^2}{(\sigma_i^{\mathrm{data}})^2}$$

where x_i^{data} is the value of each experimental point for all the asymmetries and x_i^{model} is the corresponding value of the theoretical prediction. Since the model is given without errors, only the experimental errors σ_i^{data} were used in the denominator.

All the curves shown in this section display the exact point by point model prediction. In order to compare the model to the data, it is necessary to integrate over the bin size to obtain an average value equivalent to that for

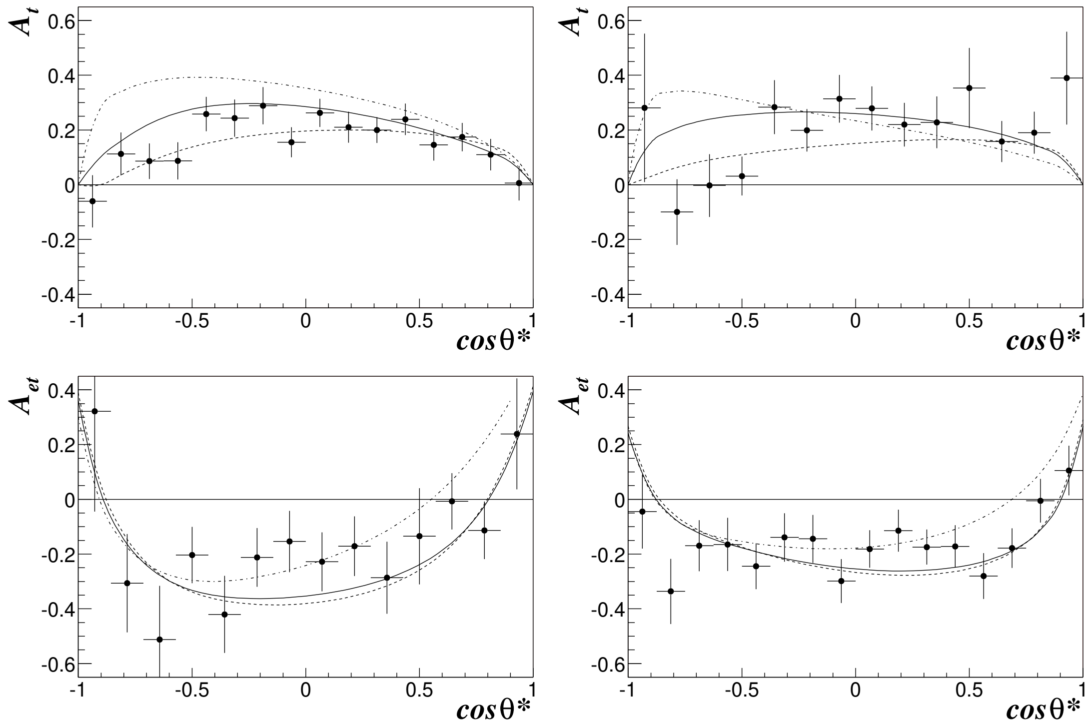

FIG. 12: Asymmetries A_t and A_{et} as a function of the center of mass angle of the pion $\cos(\theta^*)$ for 0.5 GeV$^2/c^2$ $< Q^2 <$ 0.9 GeV$^2/c^2$ (left) and 0.9 GeV$^2/c^2$ $< Q^2 <$ 1.5 GeV$^2/c^2$ (right). The curves represent the predictions from the MAID2000 model (solid), Davidson-Mukhopadhyay model (dash-dotted) and Sato-Lee model (dashed).

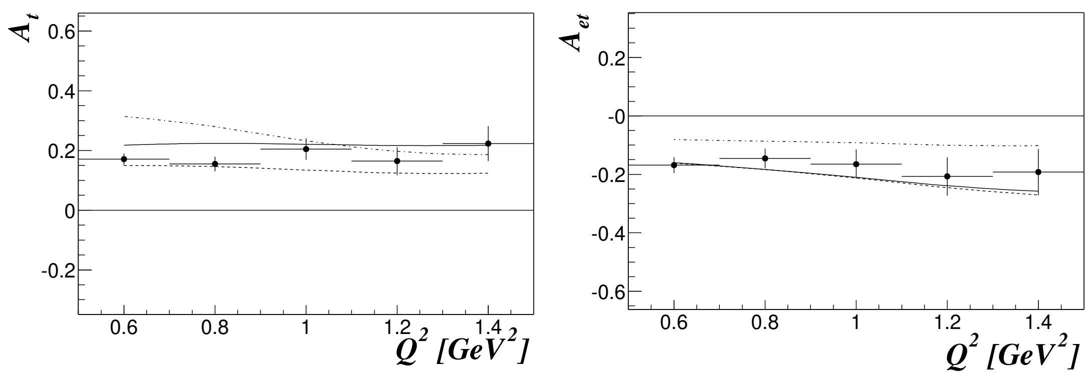

FIG. 13: Asymmetries A_t and A_{et} as a function of the momentum transfer Q^2. The curves represent the predictions from the MAID2000 model (solid black), Davidson-Mukhopadhyay model (dash-dotted) and Sato-Lee model (dashed).

the data. In other words, the models were histogrammed into bins corresponding to the same bin sizes as the data. Each experimental point is counted as a degree of freedom and the comparison yields the results listed in Table VII.

VI. SUMMARY.

Target and double spin asymmetries for the $\Delta(1232)$ decaying into p and π^0 were extracted as a function of the pion center of mass angles θ^*, ϕ^* and the momentum transfer Q^2. The double spin asymmetries for the exclusive channel are the first measurement of this kind. Comparison with some of the existing theories was performed and some sensitivity to the different models was observed. A χ^2 comparison shows (see table VII) that

TABLE VII: χ^2 comparison between the data and the four models.

Model	A_t (ndf=102)	A_{et} (ndf=65)
MAID2000	183.4	68.6
MAID98	165.2	87.2
SL	110.2	78.6
DM	418.7	107.6

the model with the best agreement with the data is the dynamical model by Sato and Lee, while the effective Lagrangian model by Davidson and Mukhopadhyay does not give a good description. The two models, MAID98 and MAID 2000, were found very similar to each other and in reasonable agreement with the data.

The results of the χ^2 comparison for the MAID and Sato-Lee models are very similar for the double spin asymmetry A_{et}. The differences in the total χ^2 are primarily determined by the comparison with the single spin asymmetry A_t. On one hand the double spin asymmetry is characterized by the term $|M_{1+}|^2$, which dominates the pion cross section, suggesting that all the models describe the $\Delta(1232)$ reasonably well. The target asymmetry on the other hand is the imaginary part of interference terms and therefore depends on multipoles such as E_{0+}, S_{0+}, M_{1+} and S_{1-}, which have larger uncertainties in the models. In this respect the SL model considers all the second order processes, whereas MAID makes approximations for these terms. A more recent approach by the MAID group (DMT) [35] accounts for these second order processes. The DM model does not include tails from higher resonances, limiting the background description even further.

In the spring of 2000 an additional 25×10^9 double polarization triggers with range of beam energy from 1.6 to 5.7 GeV were collected, concluding data taking for this experiment. This increase of a factor 10 in the number of events, and the expanded Q^2 range of the new data, should improve the sensitivity of the experiment to the different models and allow us to constrain the various theories.

APPENDIX: MULTIPOLE NOTATION

The cross section for electro-production in equations 7 can also be written as a combination of Legendre Polynomials and their 1st and 2nd derivatives. The coefficients of this expansion are the multipoles: $E_{l\pm}$,$M_{l\pm}$ and $S_{l\pm}$ [4]. The multipoles characterize the excitation mechanism (electric (E), magnetic (M) and coulomb or scalar(S) type of photon) and the angular momentum of the final state πN. $l\pm$ refers to a state with a πN relative angular momentum l and total angular momentum $J = l \pm \frac{1}{2}$.

ACKNOWLEDGMENTS

We thank T.S. Lee and L. Tiator for the valuable help with the interpretation of the results.

We acknowledge the efforts of the staff of the Accelerator and Physics Division at Jefferson Lab for making this experiment possible. This work was supported by the U. S. Department of Energy, The U. S. National Science Foundation, The French Commissariat a l'Energie Atomic, the Italian Istituto Nazionale di Fisica Nucleare.

[1] T. Sato and T. S. Lee, Phys. Rev. C **63**, 055201 (2001).
[2] T. Sato and T. S. Lee, Phys. Rev. C **54**, 2660 (1996).
[3] Kamalov and S. Yang, Phys. Rev. Letters **83**, 4494 (1999).
[4] G. Knochlein, D. Drechsel, and L. Tiator, Z. Phys. A **352**, 327 (1995).
[5] D. Drechsel, O. Hanstein, S. S. Kamalov, and L. Tiator, Nucl. Phys. A **645**, 145 (1999).
[6] R. M. Davidson, N. C. Mukhopadhyay, and R. S. Wittman, Phys. Rev. D **43**, 71 (1991).
[7] I. Aznauryan and S. Stepanyan, Phys. Rev. D **59**, 54009 (1999).
[8] S. Capstick and B. D. Keister, Phys. Rev. D **51**, 3598 (1995).
[9] F. Cardarelli et al., Physics Letters **B371**, 7 (1996).
[10] V. M. Belyaev and A. V. Radyushkin, Phys. Rev. D **53**, 6509 (1996).
[11] P. Stoler, Phys. Rev. D **65**, 053013 (2002).
[12] L. L. Frankfurt, . V. Polyakov, M. Strikman, and M. Vanderhaeghen, Phys. Rev. Lett. **84**, 2589 (2000).
[13] C. E. Carlson and J. L. Poor, Phys. Rev. D **38**, 2758 (1988).
[14] G. Blanpied et al., Phys. Rev. C **64**, 025203 (2001).
[15] R. Beck et al., Phys. Rev. Lett. **78**, 606 (1997).
[16] F. Kalleicher, U. Dittmayer, R. W. Gothe, H. Putsch, T. Reichelt, B. Schoch, and M. Wilhelm, Z. Phys. A **359**, 201 (1997).
[17] V. V. Frolov et al., Phys. Rev. Lett. **82**, 45 (1999).
[18] K. Joo et al., Phys. Rev. Lett. **88**, 122001 (2002).
[19] C. Mertz et al., Phys. Rev. Lett. **86**, 2963 (2001).
[20] K. Joo et al., to be published.
[21] D. Drechsel and L. Tiator, J. Phys. G **18**, 449 (1992).
[22] C. K. Sinclair, CEBAF-PR-89-002.
[23] M. Borghini, CERN-68-32, CERN Yellow report (1968).
[24] A. Abragam, *The principle of nuclear magnetism* (Oxford Claredon Press, 1961).
[25] T. Niinikoski, Nucl. Instr. Meth. **116**, 269 (1974).
[26] D. G. Crabb and D. B. Day, Nucl. Instrum. Meth. A **356**, 9 (1995).
[27] *CEBAF conceptual design report for experimental equipment* (1990).
[28] G. Adams et al., *The CLAS detector*, to be submitted to Nucl. Instr. and Meth.
[29] G. Adams et al., Nucl. Instrum. Meth. A **465**, 414 (2001).

[30] M. Amarian et al., Nucl. Instrum. Meth. A **460**, 239 (2001).
[31] A. Biselli, Ph.D. thesis, Rensselaer Polytechnic Institute (2002).
[32] T. W. Donnelly and A. S. Raskin, Annals Phys. **169**, 247 (1986).
[33] M. K. Jones, Phys. Rev. Lett. **84**, 1398 (2000).
[34] L. W. Mo and Y. S. Tsai, Rev. Mod. Phys. **41**, 205 (1969).
[35] S. S. Kamalov, G. Y. Chen, D. Drechsel, and L. Tiator, Phys. Lett. B **27**, 522 (2001).